$BaZrS_3$ Chalcogenide Perovskite Thin Films by H_2S Sulfurization of Oxide Precursors

José A. Márquez[1*], Marin Rusu[1], Hannes Hempel[1], Ibbi Y. Ahmet[2], Moritz Kölbach[2], Ibrahim Simsek[1], Leo Choubrac[1], Galina Gurieva[1], Rene Gunder[1], Susan Schorr[1,3] and Thomas Unold[1*]

[1] *Department of Structure and Dynamics of Energy Materials. Helmholtz-Zentrum Berlin für Materialien und Energie GmbH, Hahn-Meitner-Platz 1, 14109 Berlin, Germany*

[2] *Institute of Solar Fuels. Helmholtz-Zentrum Berlin für Materialien und Energie GmbH, Hahn-Meitner-Platz 1, 14109 Berlin, Germany*

[3] *Institute of Geological Sciences, Freie Universitaet Berlin, Maltese St. 74-100, 12249 Berlin, Germany*

*jose.marquez_prieto@helmholtz-berlin.de

*unold@helmholtz-berlin.de

Abstract

The earth-abundant ternary compound $BaZrS_3$, which crystallizes in the perovskite-type structure, has come into view as a promising candidate for photovoltaic applications. We present the synthesis and characterization of polycrystalline perovskite-type $BaZrS_3$ thin-films. $BaZrO_3$ precursor layers were deposited by pulsed laser deposition and sulfurized at various temperatures in an argon-diluted H_2S atmosphere. We observe increasing incorporation of sulfur for higher annealing temperatures, accompanied by a red shift of the absorption edge, with a bandgap of E_g = 1.99 eV and a large absorption strength $> 10^5$ cm^{-1} obtained for the highest annealing temperature of 1000 °C. X-ray diffraction analysis and SEM indicates enhanced crystallization at the higher annealing temperatures, but no evidence for a crystalline solid solution between the $BaZrO_3$ and $BaZrS_3$ phases is found. The charge carrier sum mobility estimated from optical-pump terahertz-probe spectroscopy indicates increasing mobilities with increasing sulfurization temperature, reaching maximum values of up to ~2 $cm^2 V^{-1}s^{-1}$.

The emergence of hybrid lead-halide perovskite-based solar cells has catalyzed large interest in photovoltaic materials research in the last years. Halide perovskite-based materials have demonstrated excellent optoelectronic properties leading to high-performance solar cells, with efficiencies surpassing 25% for single-junction devices and 29% in monolithic tandems with Si.[1,2] However, the stability of these compounds and the high toxicity of lead (Pb) is currently a major concern, which may limit the exploitation of this technology in the market.

Recently, perovskite chalcogenide materials have gained increasing interest as potentially stable materials with promising optoelectronic properties owing to their structure-type. These materials have the general formula of AMX_3 with *A* being a *group II* cation (*i.e.*, Ca^{2+}, Sr^{2+}, Ba^{2+}), *M* being a *group IV* transition metal (*i.e.*, Ti^{4+}, Zr^{4+}, Hf^{4+}) and *X* for a chalcogen anion (S^{2-}, Se^{2-}). First principle calculations have predicted the stability of several chalcogenide compounds crystallizing in the perovskite-type structure, with a bandgap suitable for optoelectronic devices including $SrSn(S/Se)_3$,[3] $Sr(Zr/Hf)S_3$,[4,5] $(Ca/Sr)HfSe_3$,[5,6] $(Ba/Sr)HfS_3$,[5,7] and $BaZrS_3$.[4–6,8,9] The density functional theory predictions were confirmed experimentally in the same study for $BaZrS_3$, $BaHfS_3$, $SrZrS_3$, and $SrHfS_3$ where the authors demonstrated that the compounds crystallize in a perovskite-type structure.[4,10] $BaZrS_3$ has been overall the most researched compound experimentally,[4,8,9,11,12] being the only one of its class synthesized in the form of polycrystalline thin films.[13,14] This compound has been reported both from theory as well as experimentally to have a very high absorption coefficient near the band-edge.[4] The same study found a bandgap of 1.95 eV, and suggested that it could be an ideal candidate for future tandem devices with Si as a bottom cell.[4]

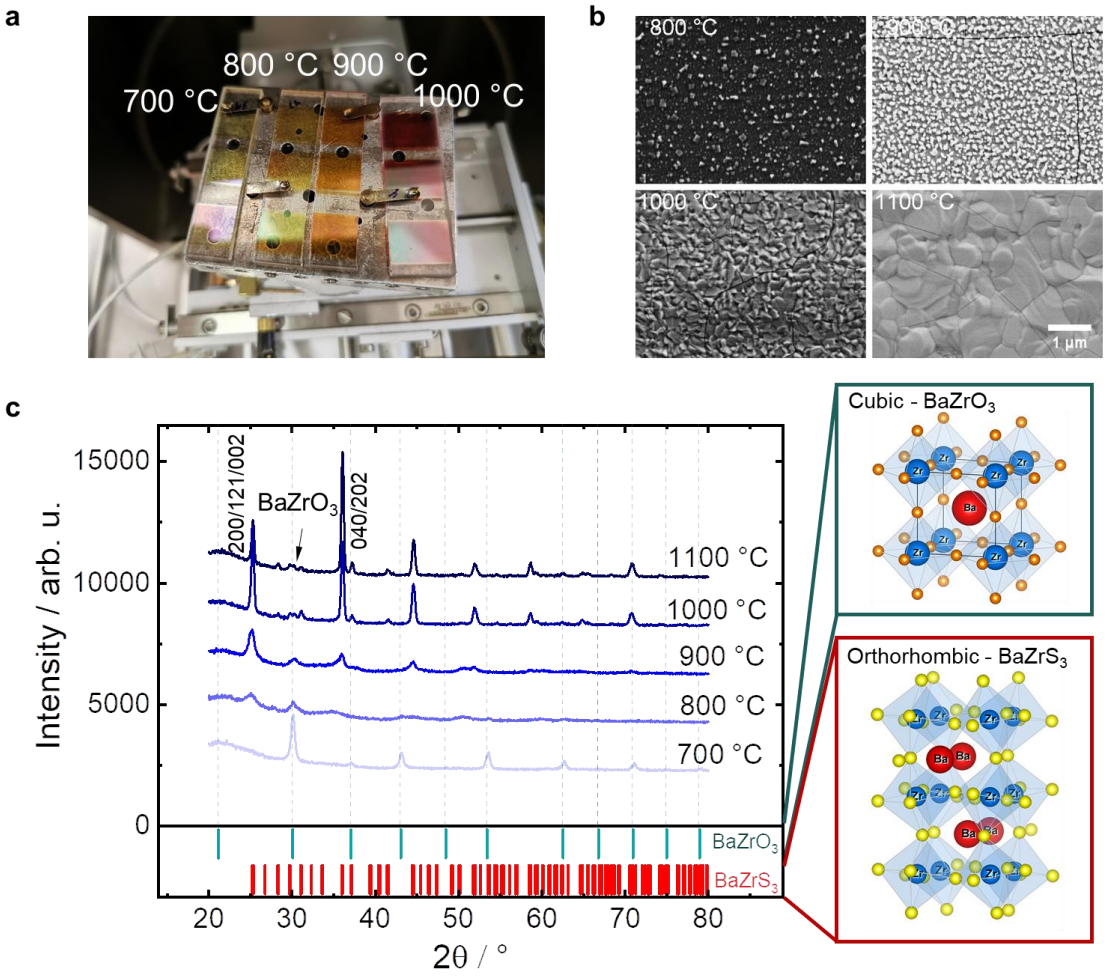

Figure 1. a) Photographic image of the $BaZrS_3$-$BaZrO_3$ samples synthesized at 700, 800, 900 and 1000 °C b) SEM top views of the $BaZrS_3$-$BaZrO_3$ films sulfurized at 800, 900, 1000 and 1100 °C for 0.5 hours. c) Diffraction patterns of the $BaZrS_3$-$BaZrO_3$ films sulfurized at different temperatures. The measurements were performed in grazing incidence configuration with an angle of 1.5° for the incidence X-ray beam. Reference positions for the Bragg reflections of $BaZrO_3$ (ICSD-90049, green) and $BaZrS_3$ (ICSD-23288, red) phases are also shown. The crystal structure of $BaZrO_3$ and $BaZrS_3$ are shown at the right-hand side of the plot where Ba atoms are represented by red spheres, Zr by blue spheres and O and S by orange and yellow spheres respectively.

Here we report the synthesis of polycrystalline $BaZrS_3$ thin films from oxide precursors. To do so, a series of ~150 nm thick amorphous Ba-Zr-O films were deposited by pulsed laser deposition (PLD) and subsequently annealed under a continuous flow of 5% H_2S(g) in argon (see supporting information for details). By varying the sulfurization temperature from 700 to 1100 °C several compositional and structural changes were observed for the films. The sulfurized films had thicknesses ranging from 150 to 250 nm (table 1). Figure 1a shows an image of the films annealed at 700, 800, 900, and 1000 °C where a visible gradual color change is appreciated. The color change goes from a pale yellow for the sample annealed at 700 °C through to more orange tones at 800 and 900 °C, and finally achieving a burgundy tone for the sample sulfurized at 1000 °C.

Rutherford Back Scattering (RBS) measurement and X-ray fluorescence (XRF) analysis revealed that there is a gradual increase in the sulfur incorporation within the films with increasing the sulfurization temperature, with the [S]/([O]+[S]) ratio saturating at around 0.85 for the sulfurizations at 1000 and 1100 °C (see table 1 and supporting information). This increase in sulfur incorporation is driven by the increase in annealing temperature since the H_2S gas flow was kept constant for all the processes. A scattered appearance of bright crystalline grains at the surface of the films is observed for the sample sulfurized at 800 °C (see Figure 1b), which increase in density for the sample sulfurized at 900 °C. The brightness difference between the crystalline grains and the dark matrix in the SEM images of these two samples suggests the coexistence of phases with different conductivities for the two lower sulfurization temperatures. The film annealed at 1000 °C shows a compact grain structure with grain sizes of about 100 nm, which further increases to the micrometer scale for the sample sulfurized at 1100 °C. Also, cracks are observed in the annealed thin films, which are likely a result of the film growth at relatively high temperatures and the

following cool-down of the samples. During that process, the thermal expansion of the $BaZrS_3$-$BaZrO_3$ films seems not to match the thermal expansion of the quartz substrate, which during cool-down induces cracks in the $BaZrS_3$-$BaZrO_3$ films.

Table 1. Sulfurization temperature, thickness, composition, bandgap E_g and sum-mobility $\sum\mu$ of the chalcogenide perovskite films.

Sulfurization temperature (°C)	Thickness / nm	[Ba]/[Zr] XRF	[S]/([S]+[O]) XRF	[a] E_g / eV	$\sum\mu$ / cm^2 V^{-1}s^{-1}
Precursor	144 ± 15	0.88 ± 0.01	0.00		--
700	151 ± 10	0.89 ± 0.01	0.25 ± 0.01	3.45 ± 0.32	--
800	226 ± 8	0.90 ± 0.01	0.53 ± 0.01	2.61 ± 0.15	0.13
900	256 ± 3	0.91 ± 0.01	0.66 ± 0.01	2.25 ± 0.15	0.35
1000	251 ± 19	0.90 ± 0.01	0.86 ± 0.01	1.99 ± 0.12	2.06
1100	202 ± 10	0.87 ± 0.01	0.84 ± 0.01	1.99 ± 0.08	2.34

[a] The bandgap E_g values are calculated from the derivative of the absorptance of the films. The errors given for the bandgap correspond to the standard deviation of a Gaussian peak fitted to the derivative of the absorptance (see supporting information).

The structural properties of the thin films were studied by grazing incidence X-ray diffraction (Figure 1c). The Bragg reflections observed in the diffractogram acquired for the sample sulfurized at 700 °C match well the reference positions for cubic perovskite-type $BaZrO_3$ (space group $Pm\bar{3}m$). The sample at 800 °C shows less intense and broader reflections at the same positions as for the 700 °C. Additionally, reflections at the positions expected for the orthorhombic perovskite-type $BaZrS_3$ (space group $Pnma$) appear in the diffraction pattern for the sample annealed at 800°C. The peaks of both phases are very broad, indicating a nanocrystalline microstructure of both phases. As the annealing temperature increases, the Bragg peaks corresponding to the $BaZrS_3$ phase become more intense and those corresponding to $BaZrO_3$ are reduced in intensity indicating that the fraction of $BaZrS_3$ in the film increases with increasing annealing

temperature. This is supported by the increase in the sulfur content in the thin film as measured by XRF (see Table 1). Sharp Bragg peaks of orthorhombic perovskite-type $BaZrS_3$ can be observed in the diffraction pattern of the thin films annealed at 1000 °C and 1100 °C. Besides that, the 110 Bragg peak of cubic perovskite-type $BaZrO_3$ is still visible but with a very small intensity indicating that the oxide phase is present in the thin film in a small amount.

Le Bail refinements of the diffraction patterns of thin films annealed at 1000°C and 1100 °C demonstrate that these data can be well described with the presence of $BaZrO_3$ ($Pm\bar{3}m$) and $BaZrS_3$ ($Pnma$) (see supporting information), and without the presence of any additional crystalline phases.[15] The line width analysis of the $BaZrS_3$ Bragg peaks measured for different incident angles proves that the thin films processed at 1100°C show higher degree of crystallinity than those processed at 1000 °C–(more details are in the supporting information).

Two main conclusions can be drawn from the structural analysis: (i) The incorporation of sulfur in the film is less energetically favorable (occurs at a major energy cost or subject to a larger energetic barrier) than the crystallization of $BaZrO_3$, which we initially observe already at an annealing temperature of 700 °C. (ii) We do not find evidence for a crystalline solid-solution $BaZr(O_xS_{1-x})_3$, since the observed Bragg peaks are centered at the expected positions of either, the oxygen-pure $BaZrO_3$ phase or the sulfur-pure $BaZrS_3$ phase. This indicates that the crystalline domains consist of either cubic $BaZrO_3$ or orthorhombic $BaZrS_3$, but the films do not contain domains where S and O are statistically intermixed within a crystalline single-phase. On the other hand, we note that for the annealing temperature 800 °C, when the sulfur/oxygen ratio of the film becomes ~50%, the crystalline peaks related to $BaZrO_3$ strongly decrease, while only one very small and broad

reflection at 25° related to $BaZrS_3$ appears. This indicates that at this temperature, when the sulfide phase forms, the $BaZrO_3$ loses crystallinity. For the annealing temperature of 900 °C, the $BaZrO_3$ reflections have almost completely disappeared, while more reflections related to $BaZrS_3$, albeit very broad, begin to appear. For temperatures above 1000 °C sharp reflections related to $BaZrS_3$ with only minor components due to $BaZrO_3$ are observed. These observations suggest that for the low annealing temperatures < 1000 °C, nanocrystalline sulfide and oxide phases are present and might be coexisting with an amorphous oxysulfide phase. This will be discussed below in relation to the optical properties measured in the films.

We applied UV-Vis spectroscopy to characterize the optical properties of the sulfurized films. The absorption coefficients α of the samples are shown in Figure 2a and indicate a decrease in the absorption onset as the sulfurization temperature increases. The shape of the absorption coefficients for the samples sulfurized at 1000 °C and 1100 °C shows good agreement with the ellipsometry study reported by Nishigaki *et al* for bulk $BaZrS_3$ samples, with an absorption onset slightly shifted to lower energies by about 100 meV.[4] In contrast, the absorption coefficient reported previously for thin films by Wei *et al.*[14] were significantly red-shifted by about 350 meV.

We note that the spectral dependence of the absorption coefficient for the films annealed at temperatures > 1000 °C cannot be well-described by the square-root dependence on energy $\alpha \sim (E - E_g)^{0.5}$, which arises from a parabolic approximation of conduction and valence band and has been found to agree well with the absorption coefficient of most direct gap compound semiconductors.[16] Here, the absorption coefficient is observed to increase more slowly at the absorption onset, which could be taken as an indication of bandgap fluctuations induced by disorder, as previously observed for other chalcogenide

semiconductors.[17,18] However, as demonstrated by Nishigaki *et al*. by a direct comparison of DFT-calculated optical absorption and experimental optical constants, the slow increase in absorption in the case of $BaZrS_3$ does not seem to arise from disorder, but rather can be explained with the nature of the valence and conduction bands and the optical transition matrix elements involved in the interband absorption.[4] In this study detailed DFT-calculations correctly predicted the experimentally observed slow increase in absorption coefficient at energies around the bandgap, without assumptions of disorder or defects. The calculations also predicted the very strong absorption coefficient > $10^5 cm^{-3}$ at energies above the bandgap, which exceeds the absorption of typical direct-gap compound semiconductors, such as CdTe or halide perovskites, by more than a factor of 3.

Figure 2b shows the bandgap values derived from the absorption measurements as a function of the S/(S+O) content in the films. Due to the slow increase of absorption near the onset, the determination of the bandgap values is challenging, as the application of a Tauc-plot implies a standard direct bandgap-type absorption coefficient. Here, we define the bandgap from the inflection point of the absorptance, which is a user independent method and does not depend strongly on the selected fitting range as is the case for the Tauc-plot method.[19] It can be seen that the bandgap E_g monotonically decreases from about 3.4 eV for the sample sulfurized at 700 °C, to 1.99 eV for the samples processed at temperatures above 1000 °C. This demonstrates a significant bandgap tunability of the material system, in accordance with reports on sulfur and oxygen-containing $BaZrS_3$ powder samples.[8] This result is somewhat surprising considering our structural analysis of the samples, which did not show the presence of a crystalline solid solution of the Ba-Zr-S-O system. We propose that the monotonically changing absorption onset might be

explained by the presence of an amorphous oxysulfide phase in the intermediate annealing temperature range, which coexists with nanocrystalline $BaZrS_3$ and $BaZrO_3$ domains. We note that bandgaps at or above 2.0 eV are well suited for photocatalytic water splitting, and thus be a possible application for this material system.

To gain insights into the recombination properties of the synthesized material we performed photoluminescence measurements at low temperatures. Figure 2c shows the PL spectrum of the $BaZrS_3$ thin film sulfurized at 1000 °C (4h), measured at 30 K. The PL spectrum is dominated by two deep broad bands, P1 and P2, centered at 1.35 eV and 1.14 eV respectively. Since these transition energies are significantly smaller than the bandgap energy, the P1 and P2 bands must be related to deep defect states in the gap. Since these transitions are very close to midgap energies, the associated defects are expected to lead to significant non-radiative recombination rates at room temperature. We note that at present we cannot exclude that the observed luminescence bands are affected by the presence of impurities in the film or oxygen-containing phases. In Fig. 2c an additional lower intensity band P3 peaking at 1.85 eV is observed, which is closer to the bandgap energy and which agrees with PL spectra previously observed in the literature for $BaZrS_3$.[13,14] At present we are not able to conclusively assign this P3 band to band-band, band-tail or to a defect related transition.

To gain insights into the charge carrier dynamics in the synthesized films, time-resolved optical-pump THz-probe (OPTP) spectroscopy measurements were performed. The derived photoconductivity transients are shown in Figure 2d indicating a fast initial decay with time constants of around $\tau_1 \approx 1$ ps. This fast initial decay is followed by a longer time constant that for the case of the sample annealed at 1000 °C is estimated at $\tau_2 \approx 30$ ps. This decay may be attributed to trapping into localized states, in which the carriers are

immobile and do not contribute to the photoconductivity. Alternatively, this decay may be attributed to a very fast recombination of charge carriers. The latter case is supported by the absence of measurable luminescence near the band edge in our samples at room temperature, which implies strong non-radiative recombination. The long component of the measured transients seems to be a phonon-related signal, which can not be attributed to electronic conductivity and will be subject to further investigation in future work. This strong non-radiative recombination might be due to the substoichiometric composition of the samples, which are Zr rich with [Ba]/[Zr] ~ 0.9 (see Table 1), while a recent report indicated that the highest luminescence yield for $BaZrS_3$ was achieved at stoichiometric compositions ([Ba]/[Zr] ~ 1).[13] However, we note that the research in this material is very pre-mature and the synthesis conditions for thin films obtained so far are expected to be far from optimized for achieving good optoelectronic properties. Further studies exploring the effect of composition and the synthesis conditions on the optoelectronic properties are needed to corroborate this.

The photoconductivity decays shown in Figure 2d are normalized by the induced carrier concentration Δn and therefore the initial amplitude corresponds to the sum of the mobility of photoexcited electrons and photoexcited holes $\sum\mu = \Delta\sigma/\Delta n/q$. The mobilities in our samples increase with increased sulfurization temperature and resulting S content. For the sample sulfurized at 800 °C ([S]/([S]+[O]) = 0.53), we measured a mobility of 0.15 $cm^2V^{-1}s^{-1}$, which increases to 0.35 $cm^2V^{-1}s^{-1}$ for the sample annealed at 900 °C ([S]/([S]+[O]) = 0.66). Samples annealed at 1000 and 1100 °C yield similar mobilities of ~2 $cm^2V^{-1}s^{-1}$, which is correlated with their similar [S]/([S]+[O]) composition. A similar increase with sulfur content was observed previously by Hall-measurements for $BaZrS_3$ thin films that

were sulfurized from oxide precursors at comparable conditions. In that study, mobility values of up to 13.7 $cm^2V^{-1}s^{-1}$ were reported for the $BaZrS_3$ thin films[14].

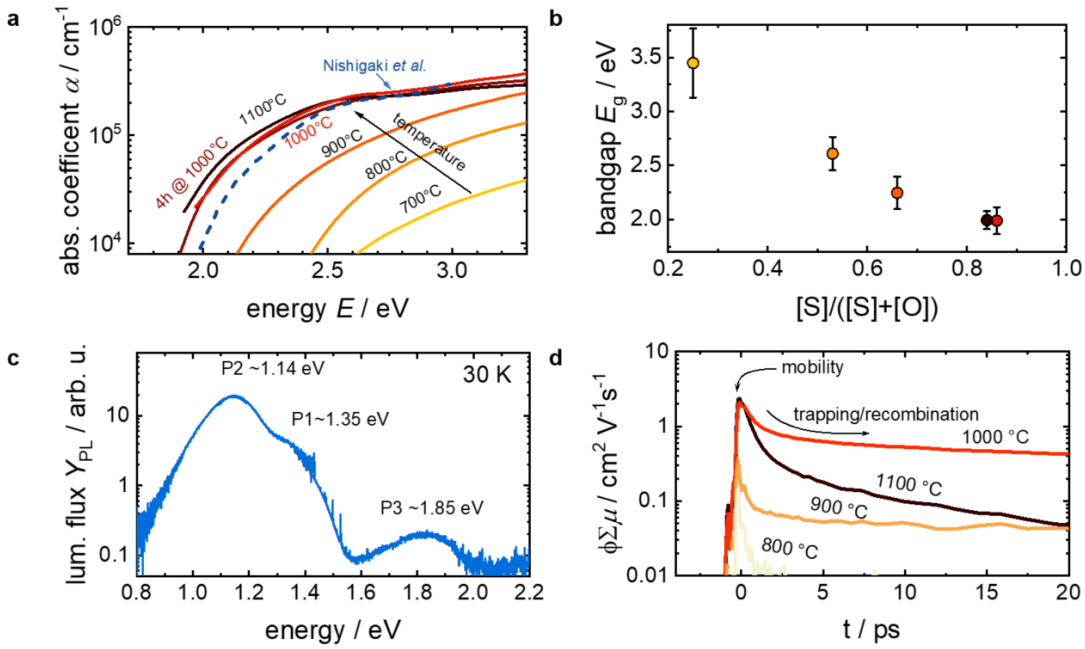

Figure 2. a) Calculated absorption coefficients for the films sulfurized for 30 minutes at 700 (light yellow), 800 (yellow), 900 (orange), 1000 (red), and 1100 °C (black-solid line). The absorption coefficient of a film sulfurized at 1000 °C for 4 hours is shown in brown. The blue dashed line shows the absorption coefficient for $BaZrS_3$ reported by Nishigaki *et al.*[4] b) Deduced average bandgap value E_g as a function of the integral [S]/([S]+[O]) ratio of the films. The error bars represent the σ value of the fitted Gaussian peak to the derivative of the absorptance (see example in supporting information). c) PL spectrum of a film sulfurized at 1000 °C (4h) measured at 30K. d) Photoconductivity decays of the sample series measured by Optical Pump Terahertz Probe measurements. The values at t = 0 correspond to the electron and hole *sum* mobility $\phi\sum\mu$ of the samples.

Still, even the highest reported mobilities in $BaZrS_3$ in the literature are below typical values found for inorganic halide perovskites such as $CsPbI_3$,[20] and almost two orders of

magnitude lower than charge carrier mobilities measured on other chalcogenide materials such as $Cu_2ZnSnSe_4$.[21] We note that at present the mobility values measured for our samples might be limited by the presence of oxygen-containing phases and that further improvements in the synthesis conditions might lead to better transport properties. However, the measured mobilities are larger than the ones found for typical metal oxides used for water splitting devices which are typically below 0.5 $cm^2V^{-1}s^{-1}$. [22,23] Such a larger mobility in combination with a bandgap of around 2 eV makes $BaZrS_3$ also a promising candidate for direct water splitting applications.

In conclusion, $BaZrS_3$-$BaZrO_3$ perovskite films were synthesized by annealing amorphous Ba-Zr-O precursors at temperatures between 700 and 1100 °C under a continuous flow of H_2S gas (5%). At 700 °C XRF measurements indicate low incorporation of sulfur, and the films mainly consist of cubic perovskite-type $BaZrO_3$. An increase of S incorporation is observed as the annealing temperature is increased reaching a maximum [S]/([S]+[O]) ratio of ~0.85. Increasing the sulfurization temperature above 1000 °C does not further red-shift the absorption onset nor increase the S incorporation. We estimate a bandgap energy E_g = 1.99 eV for the $BaZrS_3$ films synthesized at temperatures above 1000 °C. In accordance with literature, a slow increase of the absorption onset and very high absorption strength above the bandgap are observed. Low-temperature photoluminescence measurements in the sample sulfurized at 1000 °C reveal two luminescence transitions centered at 1.14 and 1.35 eV evidencing the presence of defect states within the bandgap. THz-derived charge carrier mobilities in the films reach 2 $cm^2V^{-1}s^{-1}$ for the highest sulfurization temperature. The photoconductivity transient indicates very fast recombination within a few picoseconds, which is in line with strong non-radiative recombination. The synthesis route presented here enables chalcogenide

perovskite films with tuneable bandgaps. However, to achieve single phase $BaZrS_3$ thin films, the use of oxygen-free precursor layers might be a more suitable approach.

Associated content

The Supporting Information is available free of charge on the ACS Publications website at DOI: 10.1021… Experimental methods, extended grazing incidence XRD analysis, RBS analysis, absorptivity and bandgap estimation comaprison, and fit to the OPTP transient.

Acknowledgments

We acknowledge support from the Helmholtz-Energy-Materials Foundry (HEMF) Project in providing funding for the materials synthesis facility. Lars Steinkopf is acknowledged for support with the PLD depositions. J.A.M. acknowledges Hampus Näsström and Jonathan Scragg for fruitful discussions. The authors acknowledge the Ion Beam Center at the Helmholtz-Zentrum Dresden-Rossendorf (Germany) for the possibility to perform the RBS measurements. René Heller is thanked for his RBS user support.

References

(1) Al-Ashouri, A.; Köhnen, E.; Li, B.; Magomedov, A.; Hempel, H.; Caprioglio, P.; Márquez, J. A.; Morales Vilches, A. B.; Kasparavicius, E.; Smith, J. A.; et al. Monolithic Perovskite/Silicon Tandem Solar Cell with 29% Efficiency by Enhanced Hole Extraction. *Science (80-.).* **2020**, *370* (6522), 1300–1309. https://doi.org/10.1126/science.abd4016.

(2) Best Research-Cell Efficiency Chart https://www.nrel.gov/pv/cell-efficiency.html

(3) Ju, M.-G.; Dai, J.; Ma, L.; Zeng, X. C. Perovskite Chalcogenides with Optimal Bandgap and Desired Optical Absorption for Photovoltaic Devices. *Adv. Energy Mater.* **2017**, n/a-n/a. https://doi.org/10.1002/aenm.201700216.

(4) Nishigaki, Y.; Nagai, T.; Nishiwaki, M.; Aizawa, T.; Kozawa, M.; Hanzawa, K.; Kato, Y.; Sai, H.; Hiramatsu, H.; Hosono, H.; et al. Extraordinary Strong Band-Edge Absorption in Distorted Chalcogenide Perovskites. *Sol. RRL* **2020**, *4* (5), 1900555. https://doi.org/10.1002/solr.201900555.

(5) Peng, Y.; Sun, Q.; Chen, H.; Yin, W. J. Disparity of the Nature of the Band Gap between Halide and Chalcogenide Single Perovskites for Solar Cell Absorbers. *J. Phys. Chem. Lett.* **2019**, *10* (16), 4566–4570. https://doi.org/10.1021/acs.jpclett.9b01657.

(6) Sun, Y. Y.; Agiorgousis, M. L.; Zhang, P.; Zhang, S. Chalcogenide Perovskites for Photovoltaics. *Nano Lett.* **2015**, *15* (1), 581–585. https://doi.org/10.1021/nl504046x.

(7) Hanzawa, K.; Iimura, S.; Hiramatsu, H.; Hosono, H. Material Design of Green-Light-Emitting Semiconductors: Perovskite-Type Sulfide SrHfS3. *J. Am. Chem.*

Soc. **2019**, *141* (13), 5343–5349. https://doi.org/10.1021/jacs.8b13622.

(8) Perera, S.; Hui, H.; Zhao, C.; Xue, H.; Sun, F.; Deng, C.; Gross, N.; Milleville, C.; Xu, X.; Watson, D. F.; et al. Chalcogenide Perovskites – an Emerging Class of Ionic Semiconductors. *Nano Energy* **2016**, *22*, 129–135. https://doi.org/10.1016/j.nanoen.2016.02.020.

(9) Meng, W.; Saparov, B.; Hong, F.; Wang, J.; Mitzi, D. B.; Yan, Y. Alloying and Defect Control within Chalcogenide Perovskites for Optimized Photovoltaic Application. *Chem. Mater.* **2016**, *28* (3), 821–829. https://doi.org/10.1021/acs.chemmater.5b04213.

(10) Breternitz, J.; Schorr, S. What Defines a Perovskite? *Adv. Energy Mater.* **2018**, *8* (34). https://doi.org/10.1002/aenm.201802366.

(11) Niu, S.; Huyan, H.; Liu, Y.; Yeung, M.; Ye, K.; Blankemeier, L.; Orvis, T.; Sarkar, D.; Singh, D. J.; Kapadia, R.; et al. Bandgap Control via Structural and Chemical Tuning of Transition Metal Perovskite Chalcogenides. *Adv. Mater.* **2017**, *29* (9), 16–21. https://doi.org/10.1002/adma.201604733.

(12) Clearfield, A. The Synthesis and Crystal Structures of Some Alkaline Earth Titanium and Zirconium Sulfides. *Acta Crystallogr.* **1963**, *16* (2), 135–142. https://doi.org/10.1107/s0365110x6300030x.

(13) Comparotto, C.; Davydova, A.; Ericson, T.; Riekehr, L.; Moro, M.; Kubart, T.; Scragg, J. J. S. The Chalcogenide Perovskite BaZrS3: Thin Film Growth by Sputtering and Rapid Thermal Processing. *ACS Appl. Energy Mater.* **2020**. https://doi.org/10.1021/acsaem.9b02428.

(14) Wei, X.; Hui, H.; Zhao, C.; Deng, C.; Han, M.; Yu, Z.; Sheng, A.; Roy, P.; Chen,

A.; Lin, J.; et al. Realization of BaZrS3 Chalcogenide Perovskite Thin Films for Optoelectronics. *Nano Energy* **2020**, *68*, 104317. https://doi.org/10.1016/j.nanoen.2019.104317.

(15) Le Bail, A. Whole Powder Pattern Decomposition Methods and Applications: A Retrospection. *Powder Diffr.* **2005**, *20* (04), 316–326.

(16) Pankove, J. I. *Optical Processes in Semiconductors*; Courier Corporation, 1975.

(17) Mattheis, J.; Rau, U.; Werner, J. H. Light Absorption and Emission in Semiconductors with Band Gap Fluctuations-A Study on Cu (In,Ga) Se2 Thin Films. *J. Appl. Phys.* **2007**, *101* (11). https://doi.org/10.1063/1.2721768.

(18) Gokmen, T.; Gunawan, O.; Todorov, T. K.; Mitzi, D. B. Band Tailing and Efficiency Limitation in Kesterite Solar Cells. *Appl. Phys. Lett.* **2013**, *103* (10), 103506. https://doi.org/10.1063/1.4820250.

(19) Carron, R.; Andres, C.; Avancini, E.; Feurer, T.; Nishiwaki, S.; Pisoni, S.; Fu, F.; Lingg, M.; Romanyuk, Y. E.; Buecheler, S.; et al. Bandgap of Thin Film Solar Cell Absorbers: A Comparison of Various Determination Methods. *Thin Solid Films* **2019**, *669*, 482–486. https://doi.org/10.1016/j.tsf.2018.11.017.

(20) Becker, P.; Márquez, J. A.; Just, J.; Al-Ashouri, A.; Hages, C.; Hempel, H.; Jošt, M.; Albrecht, S.; Frahm, R.; Unold, T. Low Temperature Synthesis of Stable Γ-CsPbI 3 Perovskite Layers for Solar Cells Obtained by High Throughput Experimentation. *Adv. Energy Mater.* **2019**, *9* (22), 1900555. https://doi.org/10.1002/aenm.201900555.

(21) Hempel, H.; Redinger, A.; Repins, I.; Moisan, C.; Larramona, G.; Dennler, G.; Handwerg, M.; Fischer, S. F.; Eichberger, R.; Unold, T. Intragrain Charge

Transport in Kesterite Thin Films—Limits Arising from Carrier Localization. *J. Appl. Phys.* **2016**, *120* (17), 175302. https://doi.org/10.1063/1.4965868.

(22) Kölbach, M.; Hempel, H.; Harbauer, K.; Schleuning, M.; Petsiuk, A.; Höflich, K.; Deinhart, V.; Friedrich, D.; Eichberger, R.; Abdi, F. F.; et al. Grain Boundaries Limit the Charge Carrier Transport in Pulsed Laser Deposited α-SnWO4Thin Film Photoabsorbers. *ACS Appl. Energy Mater.* **2020**, *3* (5), 4320–4330. https://doi.org/10.1021/acsaem.0c00028.

(23) Ziwritsch, M.; Müller, S.; Hempel, H.; Unold, T.; Abdi, F. F.; Van De Krol, R.; Friedrich, D.; Eichberger, R. Direct Time-Resolved Observation of Carrier Trapping and Polaron Conductivity in BiVO4. *ACS Energy Lett.* **2016**, *1* (5), 888–894. https://doi.org/10.1021/acsenergylett.6b00423.